Alternative Local Melting-Solidification of Suspended Nanoparticles for Heterostructure Formation Enabled by Pulsed Laser Irradiation

Mohammad Sadegh Shakeri, Zaneta Swiatkowska-Warkocka, Oliwia Polit, Tatiana Itina, Alexey Maximenko, Joanna Depciuch, Jacek Gurgul, Marzena Mitura-Nowak, Marcin Perzanowski, Andrzej Dziedzic, et al.

▶ **To cite this version:**

Mohammad Sadegh Shakeri, Zaneta Swiatkowska-Warkocka, Oliwia Polit, Tatiana Itina, Alexey Maximenko, et al.. Alternative Local Melting-Solidification of Suspended Nanoparticles for Heterostructure Formation Enabled by Pulsed Laser Irradiation. Advanced Functional Materials, 2023, 33 (43), pp.2304359. 10.1002/adfm.202304359 . hal-04217336

HAL Id: hal-04217336
https://hal.science/hal-04217336v1

Submitted on 28 Sep 2023

HAL is a multi-disciplinary open access archive for the deposit and dissemination of scientific research documents, whether they are published or not. The documents may come from teaching and research institutions in France or abroad, or from public or private research centers.

L'archive ouverte pluridisciplinaire **HAL**, est destinée au dépôt et à la diffusion de documents scientifiques de niveau recherche, publiés ou non, émanant des établissements d'enseignement et de recherche français ou étrangers, des laboratoires publics ou privés.

Alternative local melting-solidification of suspended nanoparticles for heterostructure formation enabled by pulsed laser irradiation

Mohammad Sadegh Shakeri[1,], Zaneta Swiatkowska-Warkocka[1], Oliwia Polit[1], Tatiana Itina[2], Alexey Maximenko[3], Joanna Depciuch[1], Jacek Gurgul[4], Marzena Mitura-Nowak[1], Marcin Perzanowski[1], Andrzej Dziedzic[5], Jarosław Nęcki[6]*

1. Institute of Nuclear Physics Polish Academy of Sciences, PL-31342 Krakow, Poland
2. Laboratoire Hubert Curien, Universite Jean Monnet, Saint-Etienne, France
3. SOLARIS NSRC, Jagiellonian University, Czerwone Maki 98, Krakow, Poland
4. Jerzy Haber Institute of Catalysis and Surface Chemistry, Polish Academy of Sciences, Niezapominajek 8, 30-239 Krakow, Poland
5. University of Rzeszów, 35-959 Rzeszów, Poland
6. University of Science and Technology, Al. Adama Mickiewicza 30, 30-059 Kraków, Poland

* Corresponding Author,
Mohammad Sadegh Shakeri (M.S. Shakeri)
Email: ms.shakeri@ifj.edu.pl
Phone No.: +48 515019092

Abstract

Phase formation by pulsed laser irradiation of suspended nanoparticles has recently been introduced as a promising synthesis technique for heterostructures. The main challenge still lingers regarding the exact mechanism of particle formation due to the non-equilibrium kinetic by-products resulting from the localized alternative, fast, high-temperature nature of the process. Here, we analyze the bond breaking/formation of copper or copper (II) interfaces with ethanol during the absorption of pulses for Cu-CuO-Cu_2O formation applicable as a hyper-electrocatalyst in ethanol oxidation fuel cells. This study includes but is not limited to, a comprehensive discussion of laser-suspension interaction for practical control of the synthesis process. We have shown that beyond the physical transitions, the local interface between dissociated ethanol and the molten sphere is responsible for the oxidative/reductive interactions resulting in the formation of catalytic-augmented Cu^{3+} by-product, thanks to the reactive bond force field molecular dynamics studies confirmed by ab-initio calculations and experimental observations.

Main

It is no exaggeration to say that the high application potential of the interaction between lasers and matter fascinates the scientific community with new applications every day. In this respect, the concept of laser-suspension interaction is not yet fully developed, but it promises a whole range of applications due to the temperature selectivity enabled by the absorption rules. When a suspension is irradiated with a laser pulse, the electromagnetic wave is locally absorbed by the suspended agglomerates, resulting in a temperature rise. Depending on their temperature, possible phase formations/transitions take place in a short time of the pulse duration. Immediately, the particles are cooled to ambient temperature by thermal equilibrium with the solvent molecules, which are transparent to the laser beam. This process is alternatively repeated during pulsed laser irradiation of suspensions (PLIS), initially known as pulsed laser melting in liquid (PLML) [1-7]. In 2007, Ishikawa et al [8] reported for the first time that unlike the laser ablation process used to produce smaller nanoparticles, PLML uses lower laser fluences and forms larger particles than the original constituents by melting. Later, an absorption model was introduced to calculate the temperature of suspended particles irradiated by a pulsed laser [9], followed by the addition of a cooling term to the model to calculate the temperature even more accurately [10]. However, these efforts facilitate the interpretation of thermodynamic phase transitions during PLIS; the undeniable role of the kinetics of the probable chemical reactions has been ignored. Here, we first attempted to investigate how the laser/suspension parameters affect particle formation during nano-pulsed laser irradiation of suspended Cu or CuO nanoparticles in ethanol by studying the thermodynamically stable phases using conventional and PLIS-based phase diagrams. The oxidation state of copper was also analyzed experimentally and theoretically to reveal the evolution of Cu-CuO-Cu_2O production as well as the possible formation of kinetic by-products. Besides, reactive bond molecular dynamics (RBMD) was used to study the kinetics of bond breaking/formation when the temperature of the ethanol-particle box is increased. In parallel, we proposed a mathematical model utilizing the laser-suspension parameters to consider the alternative particle growth during the PLIS process. We introduced the high-temperature solvent-sphere interactions, in addition to the physical phase transitions, as the main mechanisms for the PLIS synthesis of remarkable Cu-CuO-Cu_2O electrocatalysts for ethanol oxidation fuel cells. Exploring the precise role of effective laser-suspension parameters, particle temperature evolution, phase formation mechanism, and alternative particle growth not only introduces PLIS process as a preferred controllable synthesis method for heterostructures, but also gives scientists sufficient insight into its enormous potential applications.

Results

Phase formation, phase diagrams, and temperature evolution

Powders synthesized by the PLIS method (Supplementary part a) contain Cu, CuO, and Cu_2O phases according to JCPDS Nos. 003-1018, 48-1548, and 05-0667, respectively (Fig. 1a). The change in the

intensity of the peaks shows the laser-induced variation in the oxidation state of Cu-CuO-Cu_2O composite. According to the calculated phase diagrams in the Cu-O-C-H system, oxygen pressure plays an important role in the transitions between copper and its oxides ($Log\ P_{O_2} - T$ diagram) when the temperature is high enough to avoid the formation of $Cu(OH)_2$ and $CuCO_3$ phases (Fig. 1b). Moreover, the high pressure of CO ($Log\ P_{CO} - Log\ P_{O_2}$ diagram) causes the reduction of the oxide phases and the subsequent formation of metallic Cu (Fig. S1). Hence, more likely Cu, CuO, and Cu_2O and less likely $Cu(OH)_2$ and $CuCO_3$ are the thermodynamically stable phases which are able to be crystallized in this system.

To display phase diagrams with the functionality of laser/suspension parameters, the reaction pathways of Cu and CuO phases were recorded by calculating the temperature dependence of enthalpy and Gibbs free energy of the phases (Table S2 and Fig. S2). Consequently, $J\sigma_{abs}^{\lambda}(d) = m_p \Delta H$ was solved numerically and the laser fluence (J) required for all possible transitions was calculated for different sizes (D) of Cu and CuO spheres (Fig. 1c). Similarly, the dielectric constant was manipulated to show the flexible phase boundaries induced by the dynamic absorption efficiency (Fig. S3). On the other hand, the temperature profile of the particles was calculated numerically using the 4th order Rung-Kutta solution of $\frac{dE}{dt} = \frac{dE_{abs}}{dt} - \frac{dq}{dt}$ when both energy absorption and heat release are considered simultaneously (Fig. 1d). We have found that the contribution of energy absorption dominates the first and middle thirds of the Gaussian pulse, while heat dissipation tends to dominate the last third (Fig. S4). Therefore, pulse shape and pulse duration are responsible for the conservation of energy and heat dissipation, respectively. Nano-sized Cu and CuO particles experience the highest temperatures of 2843 and 2858° K, corresponding to $Cu(l) \leftrightarrow Cu(g)$ and $Cu_2O(l) \leftrightarrow 2Cu(g) + \frac{1}{2}O_2(g)$ reactions, respectively (Fig. 1e), while there is an inverse relationship between temperature and sub-micron particle size. The initial size distribution of agglomerates in the suspension is believed to be responsible for the multiphase crystallization leading to the synthesis of Cu-CuO-Cu_2O heterostructures.

Static oxidation state study

Among 9 optical phonon modes of CuO with C_{2h}^6 space group and 15 modes of Cu_2O with O_h^4 space group [11], 4 vibrational modes were observed in the Raman spectra of samples (Fig. 2a,b). The peak at 212 cm^{-1}, corresponding to $2E_u$ phonon mode, is generated by the twisting of Cu_4O tetrahedron around the c-axis of Cu_2O. There are also all three visible phonon modes of CuO, i.e., A_g mode centered at 280 cm^{-1}, B_g at 325 cm^{-1}, and $2B_g$ at 610 cm^{-1}. The T_{1u} modes of Cu_2O and/or bis-μ-oxo dimer core vibration of CuO_2^- (copper oxide III) also oscillate at 610 cm^{-1} [12]. Raman spectra showed greater formation of Cu_2O in the higher fluence irradiated CuO-ethanol samples and maximization of Cu_2O in Cu150 among Cu-ethanol samples.

A much stronger shake-up satellite accompanied by a Cu 2p peak in XPS spectra is associated with more Cu^{2+} species [13, 14]. Moreover, the absolute binding energy values (BE) of Cu 2p peaks do not allow us to distinguish between Cu^{+} and Cu^{0} oxidation states and between Cu^{2+} and Cu^{+} octahedral, since the differences between their energies are small [15-17]. In such a case, the distinction between Cu^{+} and Cu^{0} species can be derived from Wagner's Cu $2p_{3/2}$ – Cu $L_3M_{45}M_{45}$ diagram [15, 18]. Thus, to investigate the oxidation states qualitatively and quantitatively, we used information from high-resolution spectra of Cu 2p (Fig. 2c,f), Cu $L_3M_{45}M_{45}$ (Fig. 2d,g), and O 1s (Fig. 2e,h) regions simultaneously (Supplementary part c). The main photoelectron peaks of Cu 2p are accompanied by strong shake-up satellites in Cu-50 and CuO-RAW samples confirming the presence of copper mainly as Cu^{2+} species [19-22]. On the other hand, the weakest satellites are observed in the spectra obtained for Cu150 and CuO400, reflected in the smallest area of the sum of their CuO and $Cu(OH)_2$ components (Cu^{2+} content), which is less than 37 % of the total Cu 2p area. In Cu-ethanol samples, an increase in the low oxidation states (Cu^{0} and Cu^{+}) is observed with increasing laser fluence at the expense of a decrease in the Cu^{2+} components (both oxide and hydroxide). For Cu150, the (Cu^{0} + Cu^{+})/Cu^{2+} ratio reaches a maximum value of 2.9, while among CuO-ethanol samples, it is maximized at about 1.7 for CuO200 and CuO400.

The Cu K-edge absorption spectra (supplementary part d) include a pre-edge, an excrescence, and the main peak attributed to $1s \rightarrow 3d$, $1s \rightarrow 4p_z$, and $1s \rightarrow 4p$ transitions, respectively (Fig. 2i,k) [23]. Although the $1s \rightarrow 3d$ transition is forbidden according to the dipole selection rules, the pre-edge feature is defined as 3d-4p orbital mixing as well as vibronic and direct quadrupole coupling [24, 25]. The energy of the main peak decreases with laser fluence, while the excrescence energy is constant in all samples. However, the pre-edge shift behaves inconsistently, i.e., it increases for Cu-ethanol samples and decreases for CuO-ethanol samples (Table S7), which can be attributed to Cu oxidation and CuO reduction, respectively. Consequently, greater copper oxidation shifts the pre-edge to higher energies and vice versa. Linear combination fitting (LCF) of composite powders shows wall-to-wall conformance when Cu, CuO, and Cu_2O reference spectra were utilized (Fig. S6). Quantitative LCF analysis shows the enrichment of Cu_2O and the decrease of CuO with increasing laser fluence in both groups of samples. There is reasonable agreement between the quantitative results of the XPS and XANES spectra (Table S8).

Bond breaking/formation by molecular dynamics simulations

We observed the increasing traces of ethylene, methane, ethane and carbon monoxide by laser fluence in the chromatograph chamber (Table S10). These compounds were formed by dissociation of ethanol, although we know that the solvent is transparent to the laser beam. Therefore, we decided to investigate the particle-solvent interaction by means of reactive bond molecular dynamics (RBMD) simulations to support the hypothesis that phase formation during the PLIS process occurs not only

through thermodynamic phase transitions, but also through oxidation/reduction processes induced by the interactions between dissociated solvent and molten sphere (supplementary part e).

According to the RBMD simulation (Table S11), the interaction between the solvent and the solid phase starts with the absorption of ethanol at the solid surface (Supplementary Video1). In the correlated MB1 simulation box (Figs. S9 and S11), the decomposition of ethanol begins with the absorption of the separated OH^- groups on the Cu surface. The remaining C_2H_5 is decomposed to C_2H_4, followed by the formation of smaller hydrocarbons (Fig. 3a). The behavior of CuO in the MB2 simulation box, on the other hand, is different, since the decomposition of the solvent begins with the splitting off of H^+ and its subsequent adsorption on the oxide surface (Fig. 3b). The stronger tendency to react with oxygenated anions and hydrogenated cations is the main difference between the behavior of Cu and CuO heated spheres, respectively (Table S13). The reason for observing such a difference is attributed to the basic tendency of Cu^0/Cu^{2+} to be oxidized/reduced in ethanol, depending on the oxygen content of the box, which is also confirmed by DFT calculations (Supplementary part f). Thus, copper absorbs oxygen from ethanol ($2Cu + \frac{1}{2}O_2 = Cu_2O$), while ethanol absorbs oxygen from copper oxide ($C_2H_5OH + 2O_2 = 2CO_2 + 3H_2O$), both for oxidation purposes [26-31]. By changing the temperature of the simulation box (models MB3 and MB4), the only difference detected was the ethanol decomposition rate, which was found to be 0.60, 5.35, and 55.42 molecules/ps for the solvents decomposed at 1000, 1500, and 2843˚K, respectively. The reduction of the decomposition rate of ethanol is also observed when the temperatures of the solvent and the sphere are different (Fig. 3c,d). The lowest decomposition rate was observed for the model with solvent at room temperature and sphere at 2843˚K. During 125 ps of MD simulation for this model (MB6), the absorption of ethanol on the surface and its initial decomposition to $C_2H_5^+$ and OH^- are observed. Consequently, the temperature change influences the phase formation by changing the decomposition rate of the solvent. Considering the statistical analysis in terms of the new species timeline (MB7 model), oxidation evolution proceeds through (I) ethanol absorption on the Cu surface, (II) hydroxyl cleavage of ethanol, (III) formation of Cu clusters during copper melting, (IV) surface oxidation with hydrogenated compounds, (V) decomposition of C_2H_5 into smaller hydrocarbons, and (VI) net oxidation (Table S13). Ethanol decomposition for the CuO-ethanol system is accelerated compared to the Cu-ethanol system (Fig. 3e). Statistical analysis also showed that surface oxidation begins with the absorption of hydroxyl and water molecules on Cu clusters (Fig. S10). Later, the hydrogen is separated and the oxygen forms bonds with several copper atoms to achieve net oxidation (Supplementary Video 2). Time-dependent snapshots of the MB1 cross section show deep diffusion of oxygen and hydrogen compounds into the interior of the sphere, while carbon compounds tend to remain in the surface layers. The accumulation of carbon and oxygen at the surface was also observed in the HAADF-EDX map of a Cu150 particle (Fig. 3f).

Microstructure and growth of particles

Analysis of different parts of a given sample by shifting the laser focus in Raman spectroscopy revealed widespread changes in the intensity of Raman shifts (Supplementary part g). The synchronization between PLIS-based phase diagrams (Fig. 1c,e) and the size distribution of the resulting particles (Fig. 4a-h) indicated the possible crystallization of different phases, which was also confirmed by HRTEM analysis (Supplementary part h). To examine particle formation during the PLIS process in more detail, we have attempted to derive a series of equations to see how particles grow during the PLIS process (Supplementary Part j). According to this model, the agglomerates are irradiated with a laser pulse, which leads to fusion and formation of larger particles. Due to the alternative nature of pulsed laser irradiation, these particles have enough time to form new agglomerates, which with a certain probability can be irradiated by another laser pulse, resulting in new growth up to a size that can be melted by the laser beam [5]. The calculated probability of the probe (X) showed that the different sizes of Cu agglomerates are irradiated almost between 1-2 times, while CuO agglomerates are irradiated between 1-3 times (Fig. 4i,j). The calculation of $X \geq 1$ rejected the hypothesis of the presence of LCF-measured copper as the residual phase. The formation of the necking zone observed mainly in the low fluence irradiated samples (Fig. 4k-n) was also simulated by the MB9 model (Fig. 4o). Here, the atoms involved in the bond breaking/formation process move towards the center of the simulation box, while the necking zone between two spheres is observed first (Supplementary Video3). Finally, multistage modeling (models MB10 and MB11) showed a more complete dissociation of the solvent due to the increased formation of H2, H2O, CO, and C2 molecules compared to the previous stage (Fig. S13). Furthermore, solvent degradation shifts to the lower times as the number of stages increases, which is due to greater net oxidation (Fig. S14).

Possible formation of hypothetical Cu_2O_3

In some SAED patterns (Fig. 5c), we detected d-spacing around 3.25 Å, indicating a possible trace of a different oxidation state of copper [12]. A high-resolution XRD pattern also proved the existence of a characteristic peak at $2\theta=27.5^{\circ}$ (Fig. 5a) attributed to the (111) plane of the orthorhombic Cu_2O_3 phase (Fig. 5b). We found that the Cu_2O_3 phase is located at the CuO/Cu_2O interface (Fig. 5d) and/or at the surface of Cu_2O particles (Fig. S20), mainly due to the formation of areas of high oxygen content during the crystallization of Cu_2O from CuO.

Electrocatalysis of ethanol oxidation

The electrochemically active surface area (ECSA) showing hydrogen absorption region calculated from the cyclic voltammogram curves (CV) (Fig. 6a) showed the highest mass activity [32, 33] of 5065.00 cm^2/mg_{Cu} and 2037.50 cm^2/mg_{Cu} for CuO200/C and Cu200/C catalysts, respectively (Table S19). Moreover, the best catalytic properties were observed for the Cu100/C and Cu200/C catalysts.

In general, Cu-ethanol/C catalysts had greater potential for the ethanol oxidation reaction than CuO-ethanol/C catalysts (Fig. 6b), which can be attributed to the EOR consumption for CuO reduction [34, 35]. The value of the onset potential is also minimized for Cu100/C and Cu200/C catalysts (Fig. S28). As the most effective catalysts, Cu100/C and Cu200/C were investigated by in situ FTIR to reveal the products of ethanol oxidation (Fig. 6c,d). The IRRAS spectral peaks corresponding to CO_2 (complete oxidation), CO, CH_3CHO, and CH_3COOH (partial oxidation) [36, 37] are at 2360 cm^{-1}, 2100 cm^{-1}, 1340 cm^{-1}, and 1280 cm^{-1}, respectively (Fig. S29). The highest absorption was observed for CO_2 and the ratio of CO_2/CO was measured to be 43 and 1400 for Cu200/C and Cu100/C catalysts, respectively (Fig. 6c,d and Table S19). Compared to the Cu200/C catalyst, the Cu100/C catalyst, which consists of smaller particles (larger surface area), produced 4 times more CO_2 and about 10 times less CO, making it the most effective catalyst among all samples (Table S21). The Cu100/C catalyst retains its full oxidation potential even after 12 hours, which was not observed for Cu200/C. Apart from the surface area and compositional changes that made the 27.5%Cu-19.2%CuO-53.3%Cu_2O sample the optimal electrocatalyst, the remarkable electrocatalysis measured here is also attributed to the role of Cu^{3+} ions on the surface of the particles. The higher surface oxide (Cu^{3+}) in transition metal oxides (TMOs) and also the accumulation of charge carriers in the TMO heterojunctions facilitate the adsorption of alcohol, the desorption of decomposed molecules and the cleavage of the C-H bond by lowering the kinetic barrier [38, 39].

Discussions

Suspended agglomerates are heated by the energy absorption of a laser pulse according to their absorption efficiency, which is defined by the ratio between the wavelength of irradiation and the absorption cross section calculated according to the Mie theory. The absorbed energy is directly proportional to the laser fluence and the surface area of the agglomerate. On the other hand, the pulse factors influence the temperature development, so that the pulse shape is responsible for heat conservation, while the pulse duration controls the heat release. Cooling of the particles and re-agglomeration of the irradiated particles occurs in the time between pulses by synergistic agitation of the suspension. In addition, pulse repetition affects particle growth by changing the probability of the probe. The heating-cooling process is repeated depending on the probability of the probe in the system, resulting in alternative particle growth limited by the melting possibility of agglomerates. The size distribution depends on the solvent molecules, the initial size of the nanoparticles and the slurry, which determines the temperature gradient of the agglomerates. More importantly, the temperature of agglomerates not only determines their thermodynamically stable phases, but also affects the rate of oxidation/reduction processes during interfacial solvent-particle interactions.

Although the solvent bath is at ambient temperature, the kinetic energy of the molecules coming into contact with the surface of the heated particles is very high, resulting in the bond breaking/formation at the interface between the dissociated solvent and the heated particles. The dissociated species

diffuse into the sphere where the oxidation/reduction reactions take place according to their nature. In ethanol, the oxygen-hydrogen compounds diffuse deep into the particles, while larger carbon compounds tend to reside in the layers near the interface. So while the inner part of a particle has more to do with oxidation and physical transitions, the outer part is more controlled by chemical oxidation/reduction reactions that lead to the formation of kinetic byproducts. Here, experimental observations confirmed by DFT and MD simulations showed the formation of a higher oxidation state of copper, i.e., Cu^{3+}, due to the enrichment of oxygen in the CuO-Cu_2O interface and/or on the surface of the particles, resulting in the observation of excellent electrocatalysis in the ternary Cu-CuO-Cu2O catalyst. The presented optimal catalyst is able to retain its potential for complete ethanol oxidation even after 12 hours of use. The present novel study dealing with the comprehensive laser-suspension interaction not only provides a basis for heterostructure synthesis by PLIS, but also opens the knowledge gate to the perspective of the discipline.

Methods

Raw materials, suspension preparation, and irradiation process

Cu (US Research Nanomaterials, 40 nm average size, 99.9% purity, and 5 mM) or CuO (Sigma Aldrich powder, 50 nm average size, 99.5% purity, and 5 mM) nanoparticles (NPs) were dispersed in ethanol (POCH solvent, 99.8% purity) medium to prepare suspensions with a concentration of 0.0027 gr/liter. 15 ml of the resulting suspension was ultrasonically mixed and transferred to a sealed cell with a quartz window transparent to 523 nm wavelength. Then the mixture was irradiated with an unfocused pulsed laser beam generated by a Nd:YAG laser operating in second harmonic mode at a wavelength of 532 nm and a repetition rate of 10 Hz. Energy densities of 50, 100, 150, and 200 mJ/cm^2.pulse for Cu-ethanol and 100, 200, 300, and 400 mJ/cm^2.pulse for CuO-ethanol samples were used to irradiate colloidal suspensions for 60 minutes (Table S1). Ultrasonic agitation was used during irradiation to prevent undesirable sedimentation of suspended particles/agglomerates.

Characterizations

The patterns of the crystal structure of the particles were measured with an X-ray diffractometer (XRD, PANalytical X'Pert Pro). The detection was performed with Cu Kα (α = 1.54 Å) radiation at an operating current and voltage of 30 mA and 40 kV, respectively.

The WITec confocal Raman microscope (CRM alpha 300R), equipped with a λ = 532 nm laser and an Olympus MPLAN (100x/0.90NA) objective, was used to record Raman spectra. Data were accumulated using 60 scans with an integration time of 30 s and a resolution of 3 cm^{-1}. The monochromator of the spectrometer was calibrated on the basis of the Raman scattering line of a silicon plate (520.7 cm^{-1}). Cooper and its oxides are generally susceptible to heat-induced phase changes [11, 12]. Therefore, the spectra were recorded at very low laser power to avoid the thermal change induced by the laser (~ 0.45 mW). Baseline correction and cosmic ray removal were performed using WitecFour Plus software, version 5.3, while peak fitting analysis was performed using the software package GRAMS, version 9.2.

X-ray photoelectron spectroscopy (XPS) was performed in a multichamber UHV system with a hemispherical analyzer (SES R4000, Gammadata Scienta). A nonmonochromated AlK_α (1486.6 eV) X-ray source with an anode operating at 12 kV and 15 mA current emission was used to generate the core excitation. The spectrometer has been calibrated in accordance with ISO 15472:2001. The energy resolution of the system operating at a fixed let-through energy of 100 eV was 0.9 eV (measured as full width at half maximum for the Ag 3d 5/2 excitation line).The base pressure in the analysis chamber was about 1×10^{-10} mbar, and during the experiment, it was about 2×10^{-9} mbar. In addition, the area of sample analysis was approximately 4 mm^2 (5×0.8 mm). The binding energy (BE) of the random carbon species was used to correct the measured spectra for surface charge (C 1s line at BE = 285.0 eV). Intensities were estimated by calculating the integral of each peak (CasaXPS 2.3.23) after

subtracting the Shirley-type background and fitting the experimental curves with a combination of variable-ratio Gaussian and Lorentz lines (70:30).

The suspensions obtained from PLIS were precipitated on the sample holder and air-dried for X-ray absorption spectroscopy (XAS) analyzes. Absorbance sieves of finely powdered pure CuO, Cu2O (purchased from Merck Co.), and Cu foil were also prepared as a reference for calculating the percentage of phases using the linear combination fitting (LCF) method. The X-ray absorption spectra were recorded at the ASTRA beamline of the National Synchrotron Radiation Center in Krakow, Poland (SOLARIS). The spectrum of the Cu metal foil was accurately recorded before each XAS measurement for calibration purposes. Finally, the spectra were imported into the XAS computer software "Athena" for normalization and extraction of the data [40].

The LCF method was evaluated by mathematically fitting the X-ray absorption spectra (XAS) of the resulting composite particles with the same spectra measured for Cu, CuO, and Cu2O as reference. In this method, which uses the additive nature of the absorption of each species, the proportions of the reference spectra are added to reconstruct the spectrum of choice. However, it can be applied to XANES, XANES derivative, or EXAFS spectra; here we used it for the entire XAS range measured. The total absorption coefficient can be written as the sum of the chemical forms or species as $Sample = \sum f_i(STD_i)$. Here, "Sample" stands for the least square fit to the energy range of the sample spectrum, and f_i stands for the scaling factors applied to each corresponding standard spectrum (STD_i). The scaling factor determined from the LCF indicates the proportion of the individual phases in the analyzed sample. The subroutine of LCF was created with the software Athena (XAS data analysis). Here we performed LCF by fitting the normalized μ(E) spectrum of the composite samples over the reference spectra from 8900 to 9300 eV. The relative weights of the species can vary from 0 to 1 and the absorption edge energies are kept fixed during the analysis.

The hydrodynamic diameter of Cu and CuO nanoparticles was measured by dynamic light scattering (DLS) using a Malvern Zetasizer Nano- ZS instrument equipped with a He-Ne laser (λ = 633 nm) and operated at a backscattering angle of 173°.

The morphology of the synthesized particles was observed using a scanning electron microscope (Hitachi S4800 and Tescan Vega3). In addition, the average particle size was determined by measuring the diameters of 50 particles from each SEM image using ImageJ software.

The high-resolution images, selected area electron diffraction (SAED) patterns, and EDS-chemical maps were evaluated by a transmission electron microscopy (TEM, FEI Tecnai F20, 200 kV).

Thermodynamic and thermal calculations

The calculations of the thermodynamic equilibrium in the Cu-O-C-H system were carried out with the HSC Chemistry package (ver. 10.x, https://www.hsc-chemistry.com/). This software is also used for accurate calculation of Cp and enthalpy at different temperatures. The reaction pathways of heated Cu and CuO were also extracted from the Gibbs free energy and enthalpy diagrams from HSC Chemistry.

Heating-melting-vaporization model

There is a relationship between the laser fluence, the absorption cross section, the particle weight and the enthalpy of the particles as,

$$J\sigma_{abs}^{\lambda}(d) = m_p \Delta H \quad (1)$$

Where, J (J.cm^{-2}pulse^{-1}) is the laser fluence, σ_{abs}^{λ} (cm^2) is the absorption cross-section of particles, m_p (g) is the particle mass, and ΔH (J g^{-1}) is the enthalpy of the particles. The absorbed energy increases the temperature of the particle undergoing thermodynamic phase transitions.

To calculate the enthalpy of Cu and CuO spheres, the reaction paths must be known. When copper is heated, there are only two transitions, melting and boiling, so the enthalpy changes as follows.

$$\Delta H = \int_{T_0}^{T_m} C_P^s(T)dT + \Delta H_m + \int_{T_m}^{T_b} C_P^l(T)dT + \Delta H_b \quad (2)$$

here $C_P^s(T)$ and $C_P^l(T)$ (J g^{-1}K^{-1}) are the heat capacities of solid and liquid Cu. Similarly, ΔH_m and ΔH_b (J g^{-1}) are the latent heat of melting and boiling of Cu, which take place at T_m and T_b ($^{\circ}$K), respectively. Finally, T_0 ($^{\circ}$K) is the ambient temperature which was set to 298 $^{\circ}$K in all calculations. For CuO (copper oxide (II)), for which the reaction pathway is shown in Table S2, the enthalpy changes as follows.

$$\Delta H = \int_{T_0}^{T_{CuO(s)\rightarrow Cu_2O(s)}} C_P^{CuO(s)}(T)dT + \Delta H_{CuO(s)\rightarrow Cu_2O(s)} + \int_{T_{CuO(s)\rightarrow Cu_2O(s)}}^{T_m} C_P^{Cu_2O(s)}(T)dT + \Delta H_m +$$

$$\int_{T_m}^{T_{Cu_2O(l)\rightarrow Cu(g)}} C_P^{Cu_2O(l)}(T)dT + \Delta H_{Cu_2O(l)\rightarrow Cu(g)} \quad (3)$$

here, $C_p^{CuO(s)}$, $C_p^{Cu_2O(s)}$, and $C_p^{Cu_2O(l)}$ (J g^{-1}K^{-1}) are the heat capacities of solid CuO, solid Cu_2O and molten Cu_2O, respectively. Moreover, $\Delta H_{CuO(s)\rightarrow Cu_2O(s)}$, ΔH_m, and $\Delta H_{Cu_2O(l)\rightarrow Cu(g)}$ (J g^{-1}) are the latent heat of CuO(s)-Cu_2O(s) transition, Cu_2O fusion, and Cu_2O(l)-Cu(g) transition occurring at $T_{CuO(s)\rightarrow Cu_2O(s)}$, T_m, and $T_{Cu_2O(l)\rightarrow Cu(g)}$ ($^{\circ}$K) temperatures, respectively. Fig. S2 shows the changing trends of C_p and H for both phases. It also shows the transition temperatures used to design the reaction pathways according to the Gibbs free energy diagrams. The laser fluence is calculated as follows,

$$J = {}^{E_0}/_{A_L} \quad (4)$$

where, E_0 (J pulse^{-1}) is the pulse energy; A_L (cm^{-2}) is the cross section of the laser beam. Fig. S4 shows the pulse shape and cumulative pulse intensity used in this study. The Gaussian distribution of the pulse shape would be responsible for the heating. The change in the intensity of the laser pulse due to the propagation direction of the laser affects the heat balance, which we will explain in more detail using the heating-cooling model. The absorption cross section of particles, which is responsible for the absorption of electromagnetic radiation, is calculated by the following equation.

$$\sigma_{abs}^{\lambda}(d) = \frac{\pi d^2 Q_{abs}^{\lambda}(d)}{4} \quad (5)$$

here, d is the particle diameter and $Q_{abs}^{\lambda}(d)$ is the absorption efficiency of the particles calculated using scattering techniques (Mie theory in the case of submicron particles). The absorption efficiencies of Cu and CuO particles were calculated as a function of particle diameter using MiePlot software (ver. 4620, http://www.philiplaven.com/mieplot.htm), as shown in Fig. S3. The optical parameters used in the MiePlot software are listed in Table S3.

The weight of the spheres is calculated as follows,

$$m_p = \frac{\rho_p (\pi d_p^3)}{6} \quad (6)$$

where, ρ_p (g cm^{-3}) is the particle density.

Heating-cooling model

We define a model that takes into account the heating of the particles due to the absorption of the laser beam and the simultaneous cooling due to the heat transfer with the surrounding media. In this model, only conductive heat transfer is considered, since convection around the particles is negligible in the submicrometer range. Conductive heat transfer is expressed as follows;

$$\frac{dq}{dt} = h.\pi d^2(T_t - T_\infty) \quad (7)$$

where, πd^2 is the particle surface area, T(t) is the particle temperature, T_∞ is the temperature of the surrounding liquid (298 ° K), and h (Wm^{-2}K^{-1}) is the heat transfer coefficient defined by Eq. (13) as follows,

$$h = \frac{Nu_d.K}{d} \quad (8)$$

where K is the thermal conductivity of the surrounding fluid, Nu_d is the Nusselt number, and d is the particle diameter. The Nusselt number is the ratio of convective heat transfer to conductive heat transfer. In the case of natural convection on a sphere, the Nusselt number is given by Eq. (14) as [26],

$$Nu_d = 2 + \frac{0.589 Ra_d^{0.25}}{[1+(0469/Pr)^{0.56}]^{0.44}} \quad (9)$$

here, Ra_d is the Rayleigh number and Pr is the Prandtl number. For submicron particles, the magnitude of Nusselt number is equal to 2 because the Rayleigh number is negligible in the submicron range. The values of the heat transfer coefficient for ethanol are given in Table S2.

According to the heating-cooling model, the accumulated heat energy in a particle is the difference between the laser energy absorbed by a particle and the energy dissipated by conductive heat transfer,

$$\frac{dE}{dt} = \frac{dE_{abs}}{dt} - \frac{dq}{dt} \quad (10)$$

The amount of absorbed energy as a function of pulse duration is given as follows,

$$\frac{dE_{abs}}{dt} = \frac{Q_{abs}^{\lambda}(d).\pi d^2 J(t)}{4} \quad (11)$$

Matlab software (ver. R2022a, https:// www.mathworks.com/products/new_products/latest_features.html) was used for the numerical solution of differential equation of heating–cooling model using Rung Kutta 4^{th} order derivation (Eq. 10).

Gas Chromatography (GC)

The GC analyzes were performed using an Agilent 6890N gas chromatograph. The levels of carbon dioxide, carbon monoxide, and oxygen in each sample were measured using a micro TCD detector, Porapak Q, and Molsieve 5A packed columns in heart-cutting mode. Methane, ethane, and ethylene were separated using a micropacked GG alumina column and a FID detector. For high readings of certain gas concentrations (> 100ppm), the GC was calibrated with the gas mixtures produced by Multax, and the accuracy of the concentrations was more than 2% for all gasses. Low concentrations of gasses were referred to the accepted WMO scale with the set of secondary standards. Uncertainties of GC analyzes (single standard deviation), including sampling, sample transfer, and injection repeatability, were as follows: CO_2: 0.5ppm, CO: 0.2ppm, O_2: 0.1%, CH_4: 0.1ppm, C_2H_4: 0.1ppm, and C_2H_4 (or EtO): 0.1ppm.

Reactive bond force field Molecular Dynamics

All molecular dynamics (MD) simulations were performed using the ReaxFF module of the AMS software package [41], using a reactive bond force field (RBFF) with Cu/C/H/O parameters [42]. 3-dimensional systems (Table S11) with cubic simulation boxes are constructed and the periodic boundary condition is applied in all three directions. The size of the cubic simulation boxes is adjusted accordingly to keep the density the same for all systems. The canonical ensemble (NVT) is used for all MD simulations in conjunction with the Nosé-Hoover thermostat with a damping constant of 100 fs. Prior to RBFF simulations, all systems undergo energy minimization using the conjugate gradient algorithm to optimize the initial geometric configuration, followed by NVT equilibration at 298 ˚K for 5 ps. After reaching equilibrium, a series of RBFF-MD simulations is performed for each system (Table S11). In RBFF-MD simulations, the use of high temperatures to accelerate reactions is a common strategy to overcome limited computing power [43-45]. More importantly, the present study is a comparative study of different cases, so the absolute temperature used is less important. A time step of 0.25 fs is used, which has been shown to be suitable for high temperature simulations with ReaxFF MD [43]. The binding information and dynamic trajectory are recorded every 25 fs. For species analysis, a Cutoff value of 0.3 is chosen for the bond order to detect the molecules that form during the simulation. A low Cutoff value is helpful to cover all reactions even those with very short-lived species [16]. Three parallel simulations were run for each simulation box and the average of these simulations was used for further analysis. The reaction pathways (timeline of new species) are analyzed using the Chemical Trajectory Analyzer (ChemTraYzer) scripts [46]. The visualizations of

the simulation results are generated using AMS, Visual Molecular Dynamics (VMD) and Ovito programs [47].

Growth model

The details of the particle growth model were explained in supplementary part g. Eq. (S21), Eq. (S25), and Eq. (S18) were used to calculate Fig. 4i, Table S16, and Fig. 4j, respectively.

Ab-initio calculations

Quantum Espresso (QE) software was used to calculate the electronic structure and energy minimization of Cu(111) slab-ethanol, CuO(111) slab-ethanol and Cu_2O_3 unit cell models [58-50]. DFT calculations began with atomic modeling. Then the models were relaxed by minimizing the energy of the system. The calculation of the self-consistent field (SCF) was the last step before the post-processing calculations. Post-processing calculations include but are not limited to the band gap (BG), the partial density of states, and adsorption energy. The adsorption energy (E_{ads}) was calculated as follows,

$$E_{ads} = E_{slab\text{-}molecule} - (E_{slab}+E_{molecule}) \quad (12)$$

where $E_{slab\text{-}molecule}$ is the total energy of Cu(111) and CuO(111) surface after ethanol adsorption, E_{slab} is the total energy of the Cu(111) and CuO(001) surface, and $E_{molecule}$ is the total energy of the isolated ethanol molecule.

A vacuum layer (20 Å) is also added to each slab-containing model to avoid the effect of periodicity of the structure in heterojunction. The Perdew-Burke-Ernzerhof (PBE) of the generalized gradient approximation with the Hubbard on-site potential (GGA+U) approximation was utilized as exchange and interaction potentials. The Van der Waals (vdW) correction is adopted to describe long-range vdW interactions and the dipole-dipole interaction is employed in the case of an asymmetric arrangement of species. The cut-off energy of the electronic wavefunction was 600 eV, and the k-space integration is performed according to the Monkhorst-Park scheme fitted to the reciprocal space size of the crystal structure of the models. The geometry optimization of the model is terminated when the force on each ion is not stronger than 0.05 eV. We have used the pseudopotentials Cu.rel-pbesol-dn-kjpaw_psl.0.2.UPF, O.rel-pbesol-n-kjpaw_psl.0.1.UPF, C.rel-pbesol-n-kjpaw_psl.0.1.UPF, H.rel-pbesol-kjpaw_psl.0.1.UPF from http://www.quantum-espresso.org.

In addition, the jfeff10 software (https://times-software.github.io/feff10/) was used to calculate the XAFS and XANES spectra of the probable crystallized phases in this system including Cu, CuO, Cu_2O, Cu_2O_3, $CuCO_3$, and $Cu(OH)_2$. The unit cells of the above phases were relaxed using QE and the final atomic positions were used in jfeff10 for XAS calculations.

Catalyst preparation

For the electrochemical measurements, the powders obtained from the PLIS process were placed in the functionalized Vulcan XC -72R and the functionalization of the carbon support was carried out as follows. The carbon powder (20 mg) was immersed in a 0.7 M aqueous solution of HNO_3 for 30 minutes at room temperature. The Vulcan XC-72R was rinsed with distilled water to a neutral pH and then dried at 100℃ for 10 h. Prior to addition, the carbon support was heated to 100°C for 1 h under a pure nitrogen atmosphere and oxidized to form surface functional groups. After carbon functionalization, the washed synthesized powders were dispersed in an ultrasonic bath for 30 minutes and finally applied to Vulcan XC -72R, which was added dropwise with vigorous stirring. In the last step, the mixture was mixed over a night under magnetic stirring and the obtained black powder was washed with ethanol and distilled water. Then it was dried at 80°C for 10 h.

Electrochemical measurements

For the electrochemical measurements, a BIO-LOGIC SP -200 potentiostat was used in a standard three-electrode electrochemical cell. Uniform catalyst inks were prepared by ultrasonically mixing 2 mg catalyst powder with 400 μL isopropyl alcohol, 100 μL ultrapure water, and 10 μL 5 wt% Nafion solutions for 30 minutes. Then, 10 μL of the ink suspension was applied to a polished glassy carbon electrode (GCE) to obtain the working electrode with a homogeneous thin catalyst layer after the solvent was naturally air dried. To determine the EOR activity of the catalysts, cyclic voltammetry measurements (CV) were performed in ethanol-containing solution. A standard glass cell with a Pt counter electrode and a silver chloride reference electrode was used. The electrolyte, containing 0.1 M NaOH and 0.5 M C_2H_5OH, was deoxygenated by bubbling Ar for 30 min before measurements. All potentials reported in this article were calculated with respect to the reversible hydrogen electrode (RHE) and all measurements were made at room temperature.

The Infrared Reflection Absorption Spectroscopy (IRRAS) measurements

Spectroelectrochemical ATR-FTIR in situ measurements were performed using a NicoletiS50 FT-IR spectrometer equipped with an MCT detector cooled with liquid N2, an ATR accessory with ZnSe crystal, and an electrochemical cell. The working electrodes are the same as those used in electrochemical experiments. Spectra were calculated from 64 scans with a spectral resolution of 2 cm^{-1}, in the IR range between 1200 cm^{-1} and 3000 cm^{-1}. Measurements were performed for 12 h, and the spectrometer was rinsed with Ar 1 h before the experiment. In addition, argon gas was used permanently during these 12 h. The kinetics curves of the peaks were determined for every 30 minutes. The curves were indexed for peaks corresponding to CO_2, CO, CH_3CHO, and CH_3COOH to show the dynamics of the EOR products.

Acknowledgements

This work is mostly supported by the Polish National Science Centre Program No. 2018/31/B/ST8/03043. It is also supported partially by the Polish National Science Centre Program No. 2022/06/X/ST3/01743. The computational works were done in cooperation with Prometheus Cluster, Cyfronet, AGH University of Science and Technology, Krakow using Grant No. PLG/2022/015573. The authors would like to thanks Prof. Marta Marszalek, Dr. Michal Kuprinski, and Dr. Arkadiusz Zarzycki for their support during the whole project. We also are thankful of Dr. Hossein Maleki-Ghaleh due to his scientific consultation for improvement of the scientific relevancy of the current paper. Finally, a special thanks to Prof. Zbigniew Lodziana for accepting to pre-review the paper before submission.

References

[1] Yoshie Ishikawa, Naoto Koshizaki, Alexander Pyatenko, Noriyuki Saitoh, Noriko Yoshizawa, and Yoshiki Shimizu. "Nano-and submicrometer-sized spherical particle fabrication using a submicroscopic droplet formed using selective laser heating." *The Journal of Physical Chemistry C* 120, no. 4 (2016): 2439-2446.

[2] Yoshie Ishikawa, Naoto Koshizaki, and Shota Sakaki. "Spherical particle formation mechanism in pulsed laser melting in liquid under controlled-pulse-number irradiation using a slit nozzle flow system." *The Journal of Physical Chemistry C* 123, no. 40 (2019): 24934-24942.

[3] Alexander Pyatenko, Hongqiang Wang, and Naoto Koshizaki. "Growth mechanism of monodisperse spherical particles under nanosecond pulsed laser irradiation." *The Journal of Physical Chemistry C* 118, no. 8 (2014): 4495-4500.

[4] Yoshie Ishikawa, Yoshiki Shimizu, Takeshi Sasaki, and Naoto Koshizaki. "Boron carbide spherical particles encapsulated in graphite prepared by pulsed laser irradiation of boron in liquid medium." *Applied Physics Letters* 91, no. 16 (2007): 161110.

[5] Hongqiang Wang, Naoto Koshizaki, Liang Li, Lichao Jia, Kenji Kawaguchi, Xiangyou Li, Alexander Pyatenko, Zaneta Swiatkowska-Warkocka, Yoshio Bando, and Dmitri Golberg. "Size-tailored ZnO submicrometer spheres: bottom-up construction, size-related optical extinction, and selective aniline trapping." *Advanced Materials* 23, no. 16 (2011): 1865-1870.

[6] Hongqiang Wang, Kenji Kawaguchi, Alexander Pyatenko, Xiangyou Li, Zaneta Swiatkowska-Warkocka, Yukiko Katou, and Naoto Koshizaki. "General Bottom-Up Construction of Spherical Particles by Pulsed Laser Irradiation of Colloidal Nanoparticles: A Case Study on CuO." *Chemistry–A European Journal* 18, no. 1 (2012): 163-169.

[7] M. S. Shakeri, O. Polit, B. Grabowska-Polanowska, A. Pyatenko, K. Suchanek, Mateusz Dulski, J. Gurgul, and Z. Swiatkowska-Warkocka. "Solvent-particles interactions during composite particles formation by pulsed laser melting of α-Fe2O3." *Scientific Reports* 12, no. 1 (2022): 1-15.

[8] Yoshie Ishikawa, Yoshiki Shimizu, Takeshi Sasaki, and Naoto Koshizaki. "Boron carbide spherical particles encapsulated in graphite prepared by pulsed laser irradiation of boron in liquid medium." *Applied Physics Letters* 91, no. 16 (2007): 161110.

[9] Hongqiang Wang, Masahiro Miyauchi, Yoshie Ishikawa, Alexander Pyatenko, Naoto Koshizaki, Yue Li, Liang Li, Xiangyou Li, Yoshio Bando, and Dmitri Golberg. "Single-crystalline rutile TiO2 hollow spheres: room-temperature synthesis, tailored visible-light-extinction, and effective scattering layer for quantum dot-sensitized solar cells." *Journal of the American Chemical Society* 133, no. 47 (2011): 19102-19109.

[10] Shota Sakaki, Hiroshi Ikenoue, Takeshi Tsuji, Yoshie Ishikawa, and Naoto Koshizaki. "Pulse-width dependence of the cooling effect on sub-micrometer ZnO spherical particle formation by pulsed-laser melting in a liquid." *ChemPhysChem* 18, no. 9 (2017): 1101-1107.

[11] David Tuschel. "Practical group theory and Raman spectroscopy, part i: Normal vibrational modes." *Spectroscopy* 29, no. 2 (2014): 14.

[12] Yilin Deng, Albertus D. Handoko, Yonghua Du, Shibo Xi, and Boon Siang Yeo. "In situ Raman spectroscopy of copper and copper oxide surfaces during electrochemical oxygen evolution reaction: identification of CuIII oxides as catalytically active species." *Acs Catalysis* 6, no. 4 (2016): 2473-2481.

[13] Mark C. Biesinger, Leo WM Lau, Andrea R. Gerson, and Roger St C. Smart. "Resolving surface chemical states in XPS analysis of first row transition metals, oxides and hydroxides: Sc, Ti, V, Cu and Zn." *Applied surface science* 257, no. 3 (2010): 887-898.

[14] Yonglong Shen, Meilan Guo, Xiaohong Xia, and Guosheng Shao. "Role of materials chemistry on the electrical/electronic properties of CuO thin films." *Acta Materialia* 85 (2015): 122-131.

[15] Mark C. Biesinger. "Advanced analysis of copper X-ray photoelectron spectra." *Surface and Interface Analysis* 49, no. 13 (2017): 1325-1334.

[16] Anna Białas, Kamil Rugała, Cezary Czosnek, Grzegorz Mordarski, and Jacek Gurgul. "Copper aluminum spinels doped with cerium as catalysts for NO removal." *Catalysts* 10, no. 12 (2020): 1388.

[17] Jacques Ghijsen, Liu-Hao Tjeng, Jan van Elp, Henk Eskes, Jos Westerink, George A. Sawatzky, and Marek T. Czyzyk. "Electronic structure of Cu 2 O and CuO." *Physical Review B* 38, no. 16 (1988): 11322.

[18] NIST, XPS. "Database https://srdata. nist. gov/xps/(accessed Apr 8, 2020). https://doi. org/10.18434."

[19] F. Severino, J. L. Brito, J. Laine, J. L. G. Fierro, and A. López Agudo. "Nature of copper active sites in the carbon monoxide oxidation on CuAl2O4and CuCr2O4Spinel type catalysts." *Journal of Catalysis* 177, no. 1 (1998): 82-95.

[20] Ilia Platzman, Reuven Brener, Hossam Haick, and Rina Tannenbaum. "Oxidation of polycrystalline copper thin films at ambient conditions." *The Journal of Physical Chemistry C* 112, no. 4 (2008): 1101-1108.

[21] Chun-Kwei Wu, Ming Yin, Stephen O'Brien, and Jeffrey T. Koberstein. "Quantitative analysis of copper oxide nanoparticle composition and structure by X-ray photoelectron spectroscopy." *Chemistry of materials* 18, no. 25 (2006): 6054-6058.

[22] Charles C. Chusuei, M. A. Brookshier, and D. W. Goodman. "Correlation of relative X-ray photoelectron spectroscopy shake-up intensity with CuO particle size." *Langmuir* 15, no. 8 (1999): 2806-2808.

[23] Janis Timoshenko, Deyu Lu, Yuewei Lin, and Anatoly I. Frenkel. "Supervised machine-learning-based determination of three-dimensional structure of metallic nanoparticles." *The journal of physical chemistry letters* 8, no. 20 (2017): 5091-5098.

[24] Delphine Cabaret, Amélie Bordage, Amélie Juhin, Mounir Arfaoui, and Emilie Gaudry. "First-principles calculations of X-ray absorption spectra at the K-edge of 3d transition metals: an electronic

structure analysis of the pre-edge." *Physical Chemistry Chemical Physics* 12, no. 21 (2010): 5619-5633.

[25] Rui Yang, David J. Morris, Tatsuya Higaki, Matthew J. Ward, Rongchao Jin, and Peng Zhang. "Sensitive X-ray Absorption Near Edge Structure Analysis on the Bonding Properties of Au30 (SR) 18 Nanoclusters." *ACS omega* 3, no. 11 (2018): 14981-14985.

[26] Hao Huang, Yingjie Xu, Guofu Luo, Zhuobin Xie, and Wuyi Ming. "Molecular Dynamics Study of Laser Interaction with Nanoparticles in Liquids and Its Potential Application." *Nanomaterials* 12, no. 9 (2022): 1524.

[27] Muye Feng, Xi Zhuo Jiang, Weilin Zeng, Kai H. Luo, and Paul Hellier. "Ethanol oxidation with high water content: A reactive molecular dynamics simulation study." *Fuel* 235 (2019): 515-521.

[28] Jie Wang, and Gui-Chang Wang. "Promotion effect of methane activation on Cu (111) by the surface-active oxygen species: a combination of DFT and ReaxFF study." *The Journal of Physical Chemistry C* 122, no. 30 (2018): 17338-17346.

[29] Michał Kański, Sviatoslav Hrabar, Adri CT van Duin, and Zbigniew Postawa. "Development of a Charge-Implicit ReaxFF for C/H/O Systems." *The journal of physical chemistry letters* 13, no. 2 (2022): 628-633.

[30] Tao Cheng, Hai Xiao, and William A. Goddard. "Nature of the active sites for CO reduction on copper nanoparticles; suggestions for optimizing performance." *Journal of the American Chemical Society* 139, no. 34 (2017): 11642-11645.

[31] P. Ferrin, D. Simonetti, Shampa Kandoi, E. Kunkes, James A. Dumesic, Jens Kehlet Nørskov, and Manos Mavrikakis. "Modeling ethanol decomposition on transition metals: a combined application of scaling and Brønsted− Evans− Polanyi relations." *Journal of the American Chemical Society* 131, no. 16 (2009): 5809-5815.

[32] Mark K. Debe "Electrocatalyst approaches and challenges for automotive fuel cells." *Nature* 486, no. 7401 (2012): 43-51.

[33] Silvia Duran, Marine Elmaalouf, Mateusz Odziomek, Jean-yves Piquemal, Marco Faustini, Marion Giraud, Jennifer Peron, and Cédric Tard. "Electrochemical Active Surface Area Determination of Iridium-Based Mixed Oxides by Mercury Underpotential Deposition." *ChemElectroChem* 8, no. 18 (2021): 3519-3524.

[34] Madeleine Dupont, Anthony F. Hollenkamp, and Scott W. Donne. "Electrochemically active surface area effects on the performance of manganese dioxide for electrochemical capacitor applications." *Electrochimica Acta* 104 (2013): 140-147.

[35] Xianqin Wang, Jonathan C. Hanson, Anatoly I. Frenkel, Jaw-Yong Kim, and Jose A. Rodriguez. "Time-resolved studies for the mechanism of reduction of copper oxides with carbon monoxide: complex behavior of lattice oxygen and the formation of suboxides." *The Journal of Physical Chemistry B* 108, no. 36 (2004): 13667-13673.

[36] Adzic Kowal, M. Li, Minhua Shao, Kotaro Sasaki, M. B. Vukmirovic, Junliang Zhang, N. S. Marinkovic, Ping Liu, A. I. Frenkel, and R. R. Adzic. "Ternary Pt/Rh/SnO2 electrocatalysts for oxidizing ethanol to CO2." *Nature materials* 8, no. 4 (2009): 325-330.

[37] Shanza Rauf Khan, Saira Kanwal, Muhammad Hashaam, Saba Jamil, Burhan Ullah, and Muhammad Ramzan Saeed Ashraf Janjua. "Investigation of catalytic and fuel additive applications of copper/copper (I) oxide/copper (II) oxide (Cu/CuO/Cu2O) microspheres synthesized by hydrothermal method using sucrose as template." *Materials Research Express* 7, no. 2 (2020): 025036.

[38] Aditya Prajapati, Brianna A. Collins, Jason D. Goodpaster, and Meenesh R. Singh. "Fundamental insight into electrochemical oxidation of methane towards methanol on transition metal oxides." *Proceedings of the National Academy of Sciences* 118, no. 8 (2021): e2023233118.

[39] Sharif Najafishirtari, Klaus Friedel Ortega, Mark Douthwaite, Samuel Pattisson, Graham J. Hutchings, Christoph J. Bondue, Kristina Tschulik et al. "A perspective on heterogeneous catalysts for the selective oxidation of alcohols." *Chemistry–A European Journal* 27, no. 68 (2021): 16809-16833.

[40] Bruce Ravel and Mathena Newville. "ATHENA, ARTEMIS, HEPHAESTUS: data analysis for X-ray absorption spectroscopy using IFEFFIT." *Journal of synchrotron radiation* 12, no. 4 (2005): 537-541.

[41] R. Rüger, M. Franchini, T. Trnka, A. Yakovlev, E. van Lenthe, P. Philipsen, T. van Vuren, B. Klumpers, T. Soini, AMS 2022.1, SCM, Theoretical Chemistry, Vrije Universiteit, Amsterdam, The Netherlands, http://www.scm.com.

[42] Wenbo Zhu, Hao Gong, You Han, Minhua Zhang, and Adri CT Van Duin. "Development of a reactive force field for simulations on the catalytic conversion of C/H/O molecules on Cu-metal and Cu-oxide surfaces and application to Cu/CuO-based chemical looping." *The Journal of Physical Chemistry C* 124, no. 23 (2020): 12512-12520.

[43] Kimberly Chenoweth, Adri CT Van Duin, and William A. Goddard. "ReaxFF reactive force field for molecular dynamics simulations of hydrocarbon oxidation." *The Journal of Physical Chemistry A* 112, no. 5 (2008): 1040-1053.

[44] Muye Feng, Xi Zhuo Jiang, and Kai H. Luo. "A reactive molecular dynamics simulation study of methane oxidation assisted by platinum/graphene-based catalysts." *Proceedings of the Combustion Institute* 37, no. 4 (2019): 5473-5480.

[45] Qian Mao, Adri CT Van Duin, and K. H. Luo. "Formation of incipient soot particles from polycyclic aromatic hydrocarbons: A ReaxFF molecular dynamics study." *Carbon* 121 (2017): 380-388.

[46] Malte Döntgen, Marie-Dominique Przybylski-Freund, Leif C. Kröger, Wassja A. Kopp, Ahmed E. Ismail, and Kai Leonhard. "Automated discovery of reaction pathways, rate constants, and

transition states using reactive molecular dynamics simulations." *Journal of chemical theory and computation* 11, no. 6 (2015): 2517-2524.

[47] William Humphrey, Andrew Dalke, and Klaus Schulten. "VMD: visual molecular dynamics." *Journal of molecular graphics* 14, no. 1 (1996): 33-38.

[48] P. Giannozzi, O. Andreussi, T. Brumme, O. Bunau, M. Buongiorno Nardelli, M. Calandra, R. Car, C. Cavazzoni, D. Ceresoli, M. Cococcioni, N. Colonna, I. Carnimeo, A. Dal Corso, S. de Gironcoli, P. Delugas, R. A. DiStasio Jr, A. Ferretti, A. Floris, G. Fratesi, G. Fugallo, R. Gebauer, U. Gerstmann, F. Giustino, T. Gorni, J Jia, M. Kawamura, H.-Y. Ko, A. Kokalj, E. Küçükbenli, M .Lazzeri, M. Marsili, N. Marzari, F. Mauri, N. L. Nguyen, H.-V. Nguyen, A. Otero-de-la-Roza, L. Paulatto, S. Poncé, D. Rocca, R. Sabatini, B. Santra, M. Schlipf, A. P. Seitsonen, A. Smogunov, I. Timrov, T. Thonhauser, P. Umari, N. Vast, X. Wu, S. Baroni, J.Phys.: Condens.Matter 29, 465901 (2017).

[49] P. Giannozzi, S. Baroni, N. Bonini, M. Calandra, R. Car, C. Cavazzoni, D. Ceresoli, G. L. Chiarotti, M. Cococcioni, I. Dabo, A. Dal Corso, S. Fabris, G. Fratesi, S. de Gironcoli, R. Gebauer, U. Gerstmann, C. Gougoussis, A. Kokalj, M. Lazzeri, L. Martin-Samos, N. Marzari, F. Mauri, R. Mazzarello, S. Paolini, A. Pasquarello, L. Paulatto, C. Sbraccia, S. Scandolo, G. Sclauzero, A. P. Seitsonen, A. Smogunov, P. Umari, R. M. Wentzcovitch, J.Phys.: Condens.Matter 21, 395502 (2009).
Quantum Espresso GUI

[50] P. Giannozzi, O. Baseggio, P. Bonfà, D. Brunato, R. Car, I. Carnimeo, C. Cavazzoni, S. de Gironcoli, P. Delugas, F. Ferrari Ruffino, A. Ferretti, N. Marzari, I. Timrov, A. Urru, S. Baroni, J. Chem. Phys. 152, 154105 (2020).

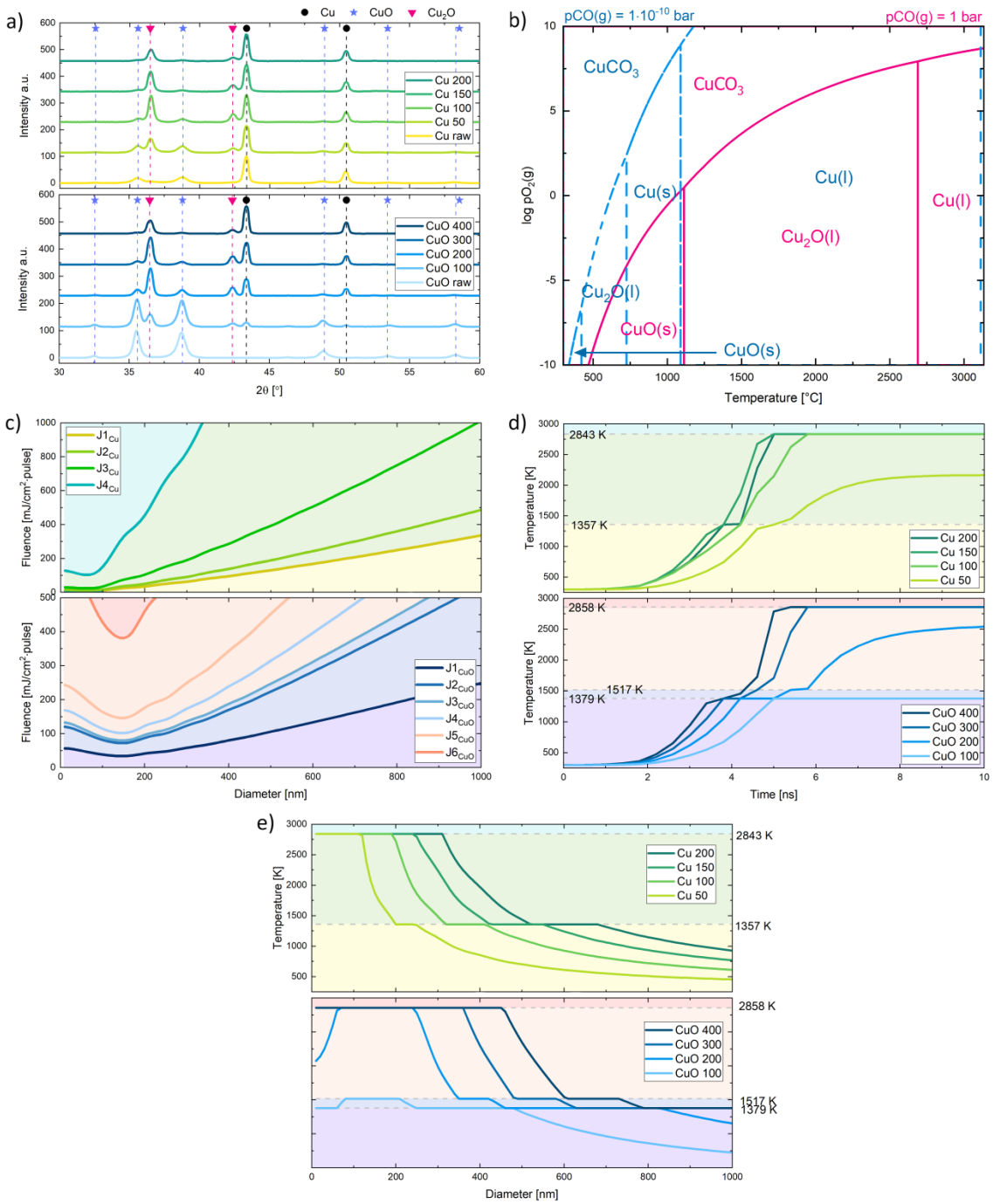
a)
Cu
CuO
Cu2O
Intensity a.u.
Cu 200
Cu 150
Cu 100
Cu 50
Cu raw
CuO 400
CuO 300
CuO 200
CuO 100
CuO raw
2θ [°]
b)
pCO(g) = 1·10-10 bar
pCO(g) = 1 bar
CuCO3
CuCO3
Cu(s)
Cu(l)
Cu(l)
Cu2O(l)
Cu2O(l)
CuO(s)
CuO(s)
log pO2(g)
Temperature [°C]
c)
J1Cu
J2Cu
J3Cu
J4Cu
Fluence [mJ/cm2-pulse]
J1CuO
J2CuO
J3CuO
J4CuO
J5CuO
J6CuO
Diameter [nm]
d)
2843 K
1357 K
Cu 200
Cu 150
Cu 100
Cu 50
Temperature [K]
2858 K
1517 K
1379 K
CuO 400
CuO 300
CuO 200
CuO 100
Time [ns]
e)
Temperature [K]
2843 K
1357 K
2858 K
1517 K
1379 K
Diameter [nm]

Fig. 1. (a) XRD patterns of Cu-ethanol and CuO-ethanol samples containing Cu, CuO and Cu_2O phases. (b) $Log\ P_{O_2} - T$ plot at $P_{CO} = 1\ and\ 1 \times 10^{-10}$ bar calculated using HSC Chemistry software for the Cu-O-C system. Cu, Cu_2O, CuO and $CuCO_3$ are the possible thermodynamically stable phases that can be crystallized in this system. (c) Plot of laser fluence versus diameter (J-D) of Cu-ethanol and CuO-ethanol calculated from Eq. (1). This diagram shows the stable phases in the different sizes of the particles after irradiation with a certain fluence of the laser pulse. (d) Temperature profile of Cu-ethanol and CuO-ethanol systems showing how the temperature of a sphere changes during absorption of a laser pulse, accompanied by simultaneous heat release. These curves were plotted for the Cu sphere with a diameter of 200 nm and the CuO sphere with a diameter of 250 nm, which were selected on the basis of the average agglomerate size of their stable suspension in ethanol. (Fig. S22). Eq. (10) and the data presented in Table S3 were also utilized to calculate the temperature profile. (e) Maximum temperature of particles as a function of size for Cu-ethanol and CuO-ethanol samples. The dashed lines show the transition temperatures. The crystallized phase of each particle is determined from its temperature after laser irradiation. For the calculation of (c), (d) and (f), the data presented in supplementary part b were used. In the diagrams in (c), (d), and (f), the light fill colors, i.e., yellow, green, and turquoise, indicate solid, liquid, and gaseous Cu, respectively, in Cu-ethanol diagrams. Purple, blue, orange and red are the illustrations of solid CuO, solid Cu_2O, liquid Cu_2O and gaseous Cu in CuO-ethanol diagrams, respectively.

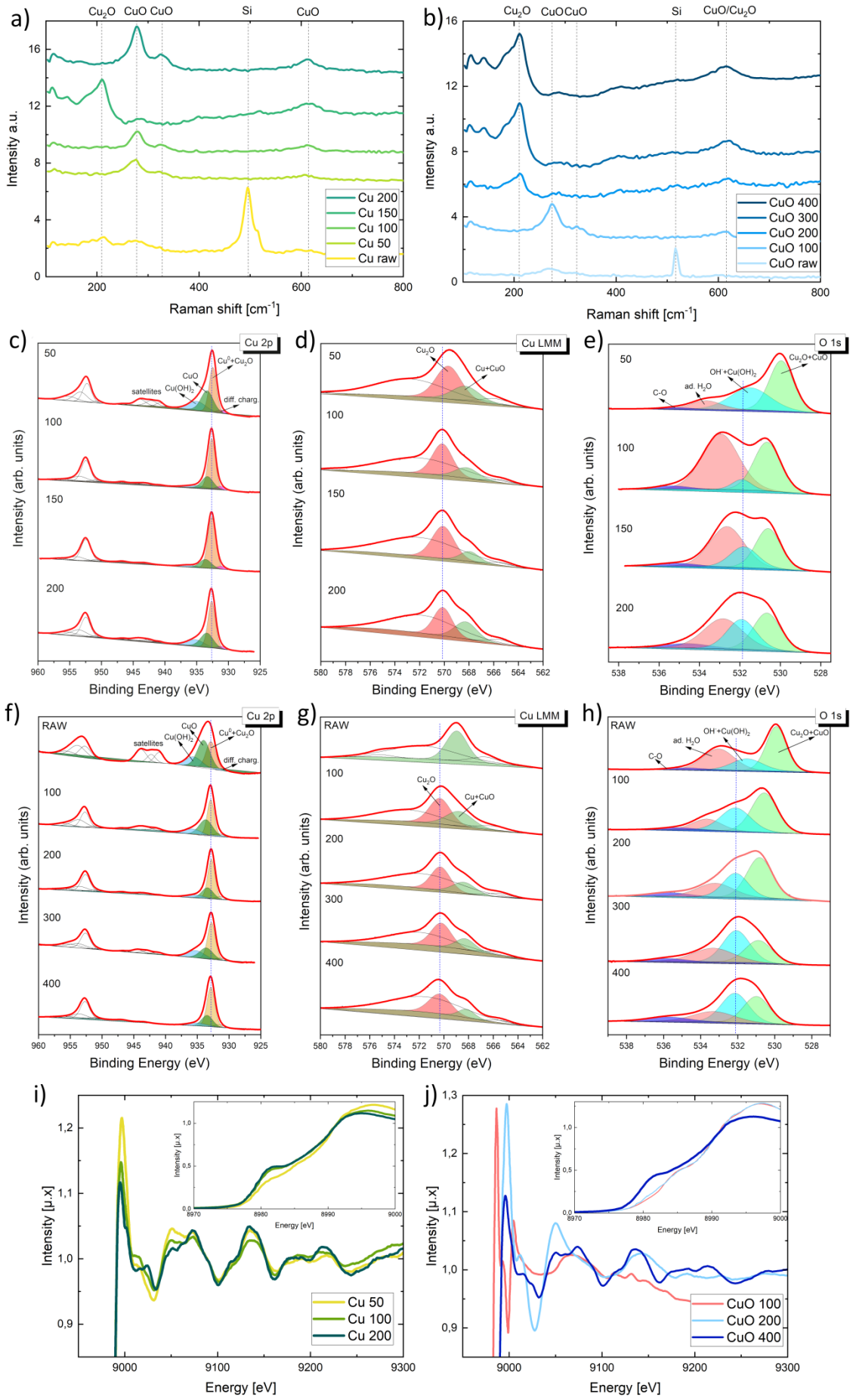
a)
Cu2O CuO CuO
Si
CuO
Intensity a.u.
Raman shift [cm-1]
Cu 200
Cu 150
Cu 100
Cu 50
Cu raw
b)
Cu2O CuO CuO
Si
CuO/Cu2O
Intensity a.u.
Raman shift [cm-1]
CuO 400
CuO 300
CuO 200
CuO 100
CuO raw
c)
Cu 2p
Intensity (arb. units)
Binding Energy (eV)
satellites
Cu(OH)2
CuO
Cu0+Cu2O
diff. charg.
d)
Cu LMM
Cu2O
Cu+CuO
e)
O 1s
C-O
ad. H2O
OH-+Cu(OH)2
Cu2O+CuO
f)
RAW
Cu 2p
g)
RAW
Cu LMM
h)
RAW
O 1s
i)
Intensity [μ.x]
Energy [eV]
Cu 50
Cu 100
Cu 200
j)
Intensity [μ.x]
Energy [eV]
CuO 100
CuO 200
CuO 400

Fig. 2. Raman spectra of (a) Cu-ethanol and (b) CuO-ethanol samples. Each sample was analyzed with more than 5 laser foci of Raman spectroscopy, and the data presented here are those obtained with the maximum repetition (Fig. S16). XPS analysis of (c) Cu 2p, (d) Cu LMM, and (e) O 1s spectra for Cu-ethanol system. XPS analysis of (f) Cu 2p, (g) Cu LMM, and (h) O 1s spectra for CuO-ethanol system. The Cu 2p, Cu LMM, and O 1s spectra were fitted with 4, 2, and 4 Gaussian doubles, respectively. The details of the quantitative analysis derived from XPS curves were presented in supplementary part c. Normalized extended X-ray absorption fine structure (EXAFS) and X-ray absorption near edge structure (XANES) for Cu K-edge spectra of (i) Cu-ethanol and (j) CuO-ethanol samples. All samples were analyzed 3 times and the average spectrum was reproduced here. Analysis of the Cu foil reference sample was performed before each measurement to meet calibration criteria. The changes in the oxidation state of the composite powders are shown in these curves. The detailed X-ray absorption spectroscopy (XAS) analysis is described in supplementary part d.

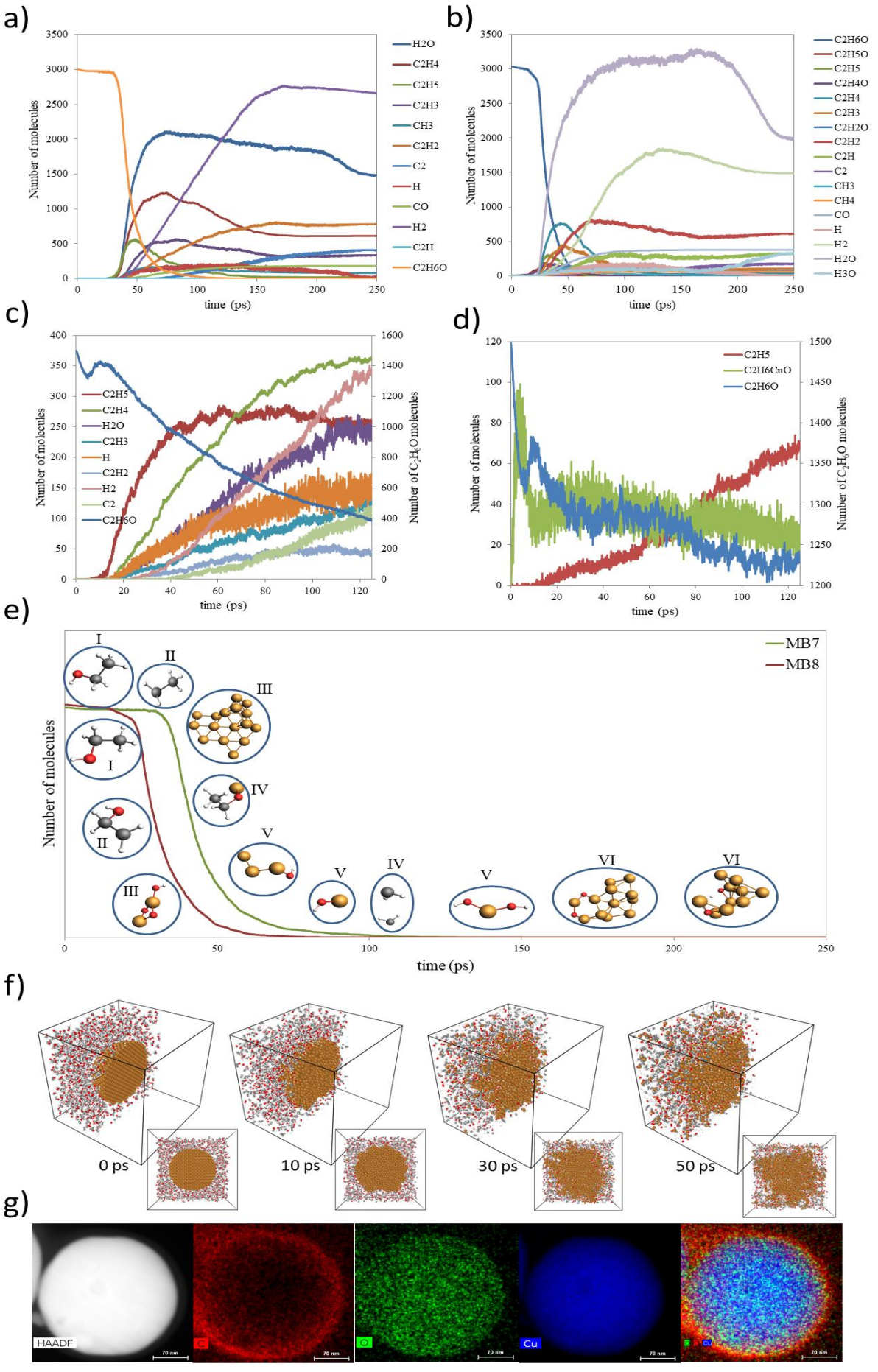
a)
Number of molecules
time (ps)
H2O
C2H4
C2H5
C2H3
CH3
C2H2
C2
H
CO
H2
C2H
C2H6O
b)
Number of molecules
time (ps)
C2H6O
C2H5O
C2H5
C2H4O
C2H4
C2H3
C2H2O
C2H2
C2H
C2
CH3
CH4
CO
H
H2
H2O
H3O
c)
Number of molecules
Number of C2H6O molecules
time (ps)
C2H5
C2H4
H2O
C2H3
H
C2H2
H2
C2
C2H6O
d)
Number of molecules
Number of C2H6O molecules
time (ps)
C2H5
C2H6CuO
C2H6O
e)
Number of molecules
time (ps)
MB7
MB8
I
II
III
IV
V
VI
f)
0 ps
10 ps
30 ps
50 ps
g)
HAADF
C
O
Cu

Fig. 3. Solvent decomposition and formation of new species from ethanol calculated using RBMD for (a) Cu-ethanol system according to RB1 model at 2843˚K, (b) CuO-ethanol system according to RB2 model at 2858˚K. The maximum temperature for each system was chosen based on the data shown in Fig. 1e. Solvent decomposition and formation of new species calculated with RBMD for the Cu-ethanol system at a sphere temperature of 2843˚K (c) with the RB5 model at a solvent temperature of 1000˚K, and (d) with the RB6 model at a solvent temperature of 298˚K. (e) Timeline of new species formation on the decomposition curves of ethanol for the Cu-ethanol and CuO-ethanol systems according to models RB7 and RB8. The species shown here were selected from thousands of new species according to their higher repetition to show the mechanism of bond breaking/formation in the systems. The evolution of the mechanism for Cu-ethanol is illustrated by (I) ethanol absorption, (II) hydroxyl cleavage, (III) formation of Cu clusters, (IV) surface oxidation, (V) further decomposition of the solvent, and (VI) net oxidation. Also shown is the absorption of ethanol, hydrogen splitting from ethanol, and formation of hydrogenated copper oxide for the CuO-ethanol system. These data were collected using the ChemTraYzer option of the AMS software based on a statistical analysis of all time steps of the simulations. (F) 3D and front snapshots of the sliced box of the MB1 model during RBMD simulation showing diffusion of species during the bond breaking/formation process. The diffusion of oxygen and hydrogen deep into the sphere and the remaining carbon compounds at the surface layer was confirmed by the EDX analysis results. (g) HAADF-EDX Analysis of a Cu_2O particle synthesized by laser irradiation of a Cu-ethanol suspension at a laser fluence of 150 mJ/cm^2.pulse (Cu150 sample). The accumulation of carbon and oxygen on the surface is clearly visible.

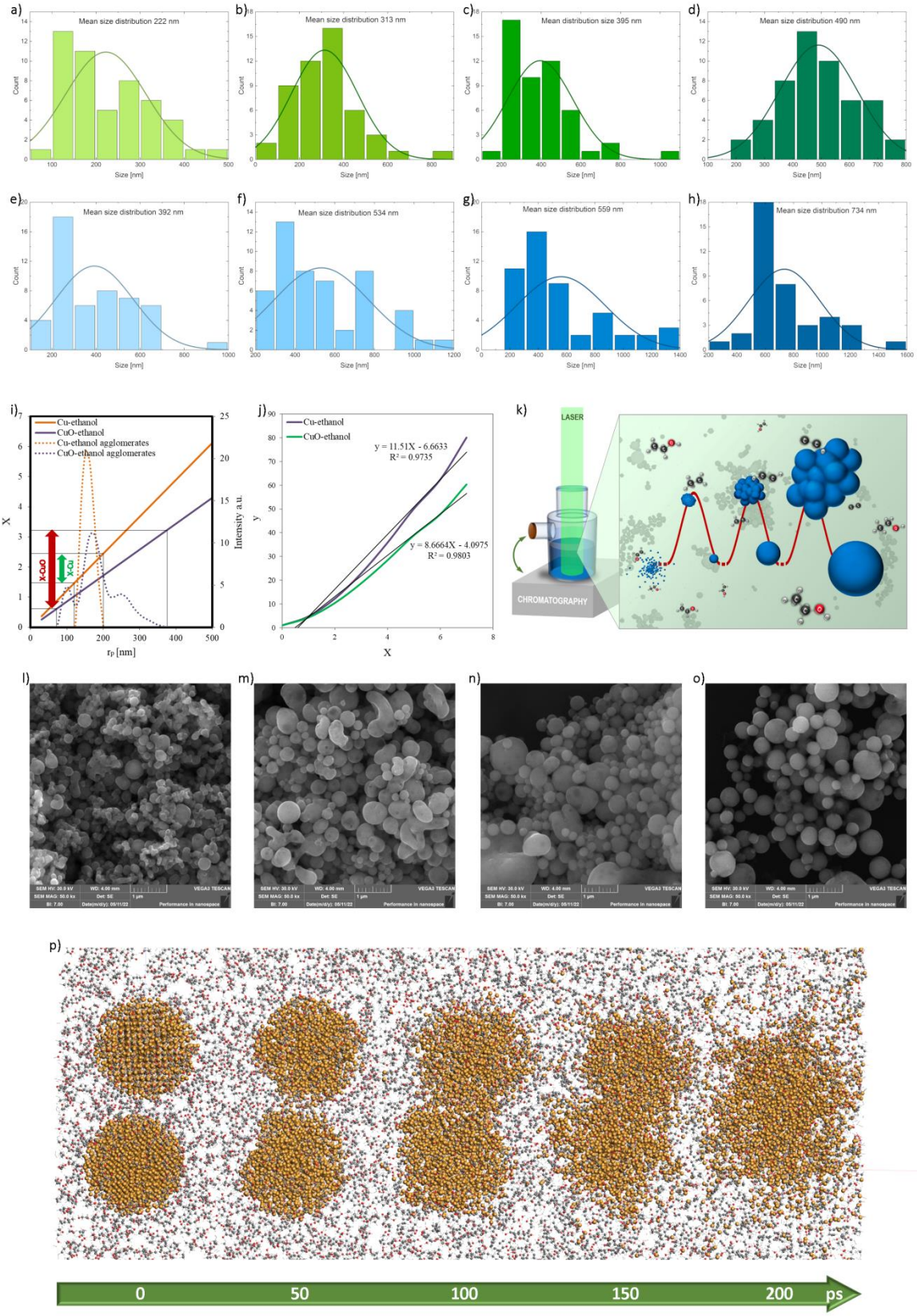
a)
Mean size distribution 222 nm
b)
Mean size distribution 313 nm
c)
Mean distribution size 395 nm
d)
Mean size distribution 490 nm
e)
Mean size distribution 392 nm
f)
Mean size distribution 534 nm
g)
Mean size distribution 559 nm
h)
Mean size distribution 734 nm
Count
Size [nm]
i)
Cu-ethanol
CuO-ethanol
Cu-ethanol agglomerates
CuO-ethanol agglomerates
X-CuO
X-Cu
X
Intensity a.u.
rp [nm]
j)
Cu-ethanol
CuO-ethanol
y = 11.51X - 6.6633
R² = 0.9735
y = 8.6664X - 4.0975
R² = 0.9803
X
y
k)
LASER
CHROMATOGRAPHY
l)
m)
n)
o)
p)
0
50
100
150
200
ps

Fig. 4. Particle size distribution of (a-d) Cu-ethanol and (e-h) CuO-ethanol samples measured from analysis of 50 particles in SEM images using ImageJ software. The increasing trend of particle size with laser fluence intensity is clearly visible in both groups of samples. (i) Probability of the probe as a function of particle size for both Cu-ethanol and CuO-ethanol systems. According to the initial size distribution of copper and copper oxide agglomerates shown by dashed lines, the probability of probe changes in the range of 1.5-2.5 for Cu-ethanol and 0.7-3.2 for CuO-ethanol samples. (j) y-X curve for Cu-ethanol and CuO-ethanol systems. $y = {r_p}/{r_{p_0}}$ as growth ratio shows that the particles in the Cu-ethanol system grow at a higher rate than in the CuO-ethanol system. (k) Schematic illustrating the growth mechanism of particles formed not only by physical phase transitions but also by interfacial reactions with the dissociated ethanol. The formation of smaller hydrocarbons in the latter pulse probe shows greater dissociation of ethanol to H_2, C_2, and CO in the absence of sufficient oxygen. SEM images of (l) Cu50, (m) Cu100, (n) Cu150, and (o) Cu200 samples showing the formation of irregular shapes with necking zones at lower laser fluences and also soundless spherical particles mainly at higher laser fluences. (p) Snapshots of the front view of the MB9 model showing the formation of necking zone between two particles during RBMD simulation.

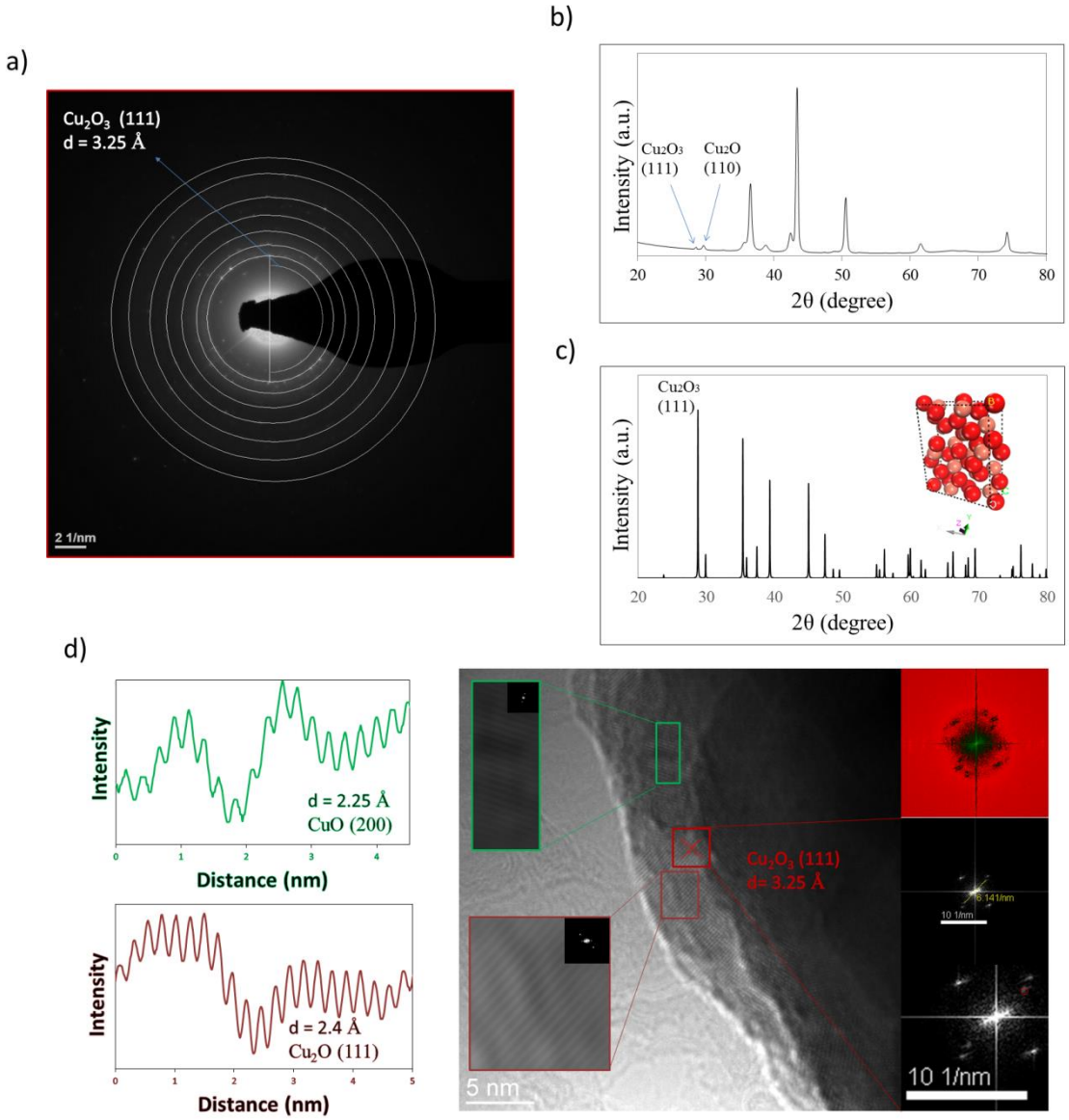

Fig. 5. (a) SAED pattern of a Cu200 particle showing the traces of Cu_2O_3 phase in a multiphase CuO and Cu_2O particle. (b) High-resolution XRD pattern of Cu200 sample analyzed at a slow rate of 0.05°/min. It shows a characteristic peak associated with the Cu2O3 (111) plane at 2θ = 27.5°. (c) Calculated XRD pattern of a relaxed orthogonal Cu_2O_3 unit cell using DFT. (d) FFT analysis of a Cu200 particle showing the crystallization of Cu_2O_3 at the interface of the CuO and Cu_2O oxides based on the calculation of the d-spacing. The enrichment of oxygen during the transition between stable copper oxides (I & II) was considered to be the reason for the crystallization of copper (III) in their interface.

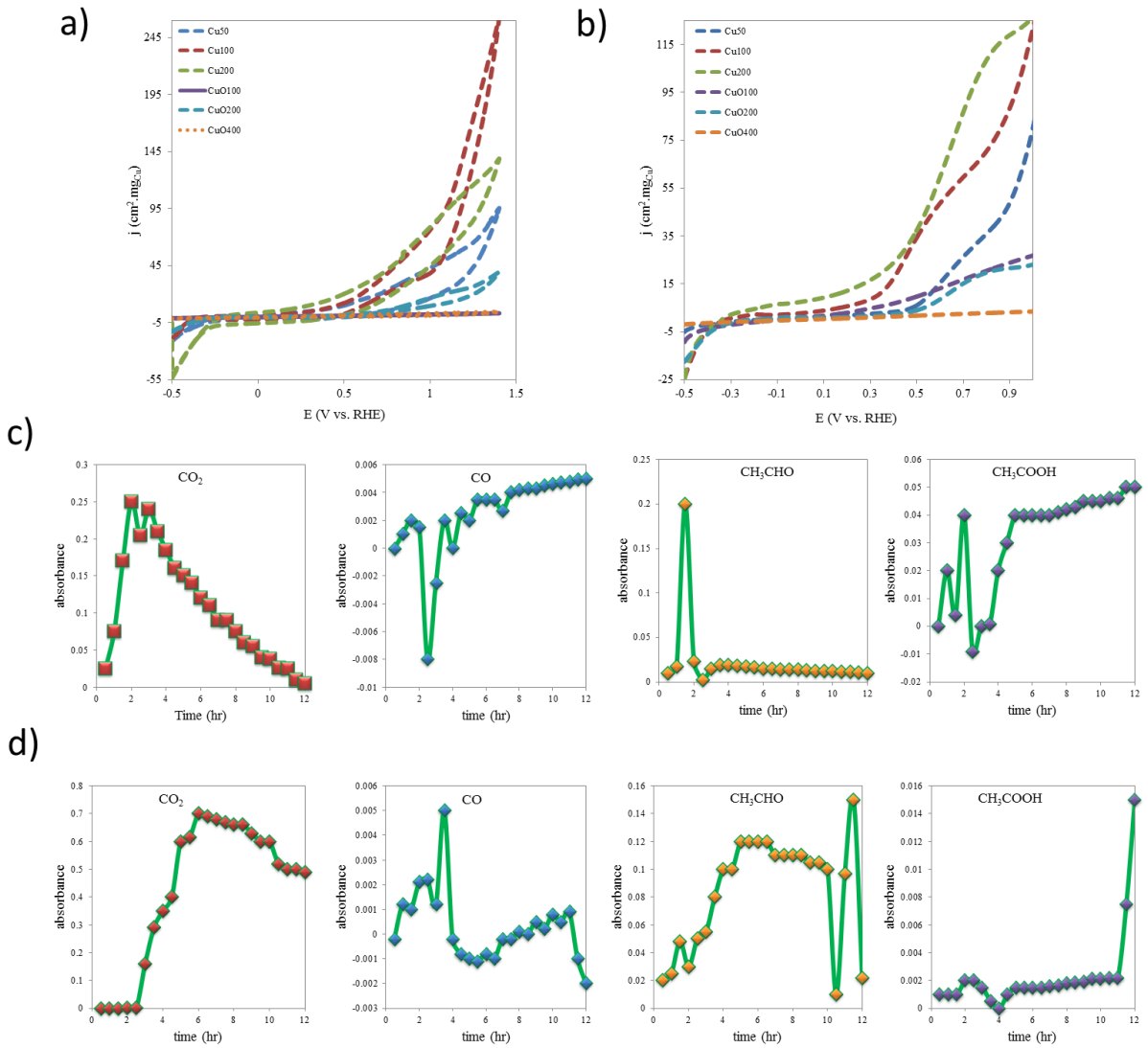

Fig. 6. (a) Cyclic voltammetry of Cu50/C, Cu100/C, Cu200/C, CuO100/C, CuO200/C and CuO400/C electrocatalysts in 0.1 M NaOH, sweep rate (50 mV/s); (b) EOR forward scan of the Cu50/C, Cu100/C, Cu200/C, CuO100/C, CuO200/C and CuO400/C catalysts. All curves were recorded in 0.1 M NaOH + 0.5 M C2H5OH solution at a scan rate of 50 mV/s at room temperature. Differences in the absorbance of peaks originating from CO_2, CO, CH_3CHO, and CH_3COOH were observed during 12 h of EOR for (c) Cu200/C and (d) Cu100/C catalysts. The dynamics of ethanol oxidation mostly shows the dominant mechanism of complete oxidation leading to enormous CO_2 production. The optimum catalyst, i.e. Cu100/C, retains its oxidation potential for 12 hours, which is not the case at all with Cu200/C. After 12 hours, Cu100/C can still be used as a catalyst for complete oxidation of ethanol, while Cu200/C is better for partial oxidation.